



Article

# Electrolyte Solvation Structure at Solid/Liquid Interface Probed by Nanogap Surface-Enhanced Raman Spectroscopy

Guang Yang, Ilia N. Ivanov, Rose E. Ruther, Robert L Sacci, Veronika Subjokova, Daniel T Hallinan, and Jagjit Nanda

ACS Nano, Just Accepted Manuscript • DOI: 10.1021/acsnano.8b05038 • Publication Date (Web): 18 Sep 2018

Downloaded from http://pubs.acs.org on September 21, 2018

#### **Just Accepted**

"Just Accepted" manuscripts have been peer-reviewed and accepted for publication. They are posted online prior to technical editing, formatting for publication and author proofing. The American Chemical Society provides "Just Accepted" as a service to the research community to expedite the dissemination of scientific material as soon as possible after acceptance. "Just Accepted" manuscripts appear in full in PDF format accompanied by an HTML abstract. "Just Accepted" manuscripts have been fully peer reviewed, but should not be considered the official version of record. They are citable by the Digital Object Identifier (DOI®). "Just Accepted" is an optional service offered to authors. Therefore, the "Just Accepted" Web site may not include all articles that will be published in the journal. After a manuscript is technically edited and formatted, it will be removed from the "Just Accepted" Web site and published as an ASAP article. Note that technical editing may introduce minor changes to the manuscript text and/or graphics which could affect content, and all legal disclaimers and ethical guidelines that apply to the journal pertain. ACS cannot be held responsible for errors or consequences arising from the use of information contained in these "Just Accepted" manuscripts.



# Electrolyte Solvation Structure at Solid/Liquid Interface Probed by Nanogap Surface-Enhanced Raman Spectroscopy

Guang Yang<sup>1</sup>, Ilia N. Ivanov<sup>1</sup>, Rose E. Ruther<sup>1</sup>, Robert L. Sacci<sup>1</sup>, Veronika Subjakova<sup>3</sup>, Daniel T.

Hallinan<sup>2</sup>\*, Jagjit Nanda<sup>1</sup>\*

KEYWORDS interface, ion solvation, gold nanoparticle, SERS, FDTD, solvation number, Liion battery

ABSTRACT Understanding the fundamental factors that drive ion solvation structure and transport is key to design high performance, stable battery electrolytes. Reversible ion solvation and desolvation are critical to the interfacial charge transfer process across the solid-liquid interface as well as the resulting stability of the solid electrolyte interphase (SEI). Herein, we report the study of Li<sup>+</sup> salt solvation structure in aprotic solution in the immediate vicinity (~ 20

<sup>&</sup>lt;sup>1</sup> Oak Ridge National Laboratory, Oak Ridge, Tennessee 37831, United States

<sup>&</sup>lt;sup>2</sup> Department of Chemical and Biomedical Engineering, Florida A&M University-Florida State University College of Engineering, 2525 Pottsdamer Street, Tallahassee, FL 32310, USA

<sup>&</sup>lt;sup>3</sup> Department of Nuclear Physics and Biophysics, Comenius University, Mlynska dolina F1, Bratislava, 84248, Slovakia

<sup>\*</sup>nandaj@ornl.gov

<sup>\*</sup>dhallinan@fsu.edu

nm) of the solid electrode-liquid interface using surface-enhanced Raman spectroscopy (SERS) from a gold nanoparticle (Au NP) monolayer. The plasmonic coupling between Au NPs produces strong electromagnetic field enhancement in the gap region, leading to 5 orders of magnitude increase in Raman intensity for electrolyte components and their mixtures namely, lithium hexafluorophosphate (LiPF<sub>6</sub>), fluoroethylene carbonate (FEC), ethylene carbonate (EC) and diethyl carbonate (DEC). Further, we estimate and compare the lithium-ion solvation number derived from SERS, standard Raman spectroscopy and Fourier transform infra-red (FTIR) spectroscopy experiments to monitor and ascertain the changes in the solvation shell diameter in the confined nanogap region where there is maximum enhancement of the electric field. Our findings provide a multi-modal spectroscopic approach to gain fundamental insights into the molecular structure of the electrolyte at the solid-liquid interface.

The growing need for energy storage systems requires batteries with high power and energy density as well as longer life and improved safety. This calls for innovations in high energy density electrode materials as well as in design of robust and efficient charge transfer interfaces without electrolyte degradation or chemical side reactions. Charge transport across the solid electrode-liquid electrolyte interface (SLI) is believed to be one of the battery charge/discharge rate limiting steps. In commercial lithium-ion batteries, the thermodynamic instability of the electrolyte at the SLI leads to formation of a passivation layer, commonly referred to as the solid-electrolyte interphase (SEI). The SEI thickness is usually in the range of tens of nanometers and it is mostly conducive to lithium-ions transport to and from the solid electrode. The composition, morphology, and structure of SEI of lithium-ion batteries have been extensively studied in the past and are not discussed in this work. The sum of the solid electrode is the solid in the past and are not discussed in this work.

The exact nature of solvation structure and ion-transport depends on multiple factors including concentration and composition of the solvent and solute as well as fundamental physical properties such as dielectric constant, polarity and nature of the chemical bonding. Probing the ion-solvation structure especially at the SLI is challenging, due to the diffraction limited spatial resolution and low sensitivity of spectroscopic techniques such as confocal micro-Raman and Fourier Transform Infrared spectroscopy (FT-IR).<sup>7</sup> In the case of confocal micro-Raman, the through-plane (depth from the sample surface) spatial resolution is generally determined by (i) the skin depth, which depends on the local electrical conductivity of the electrode and the incident laser wavelength, and (ii) the confocal plane depth of the microscope objective.<sup>8</sup> Usually it is on the order of a micron or more.<sup>9</sup> For transparent liquids such as electrolyte, as in our case, it is only limited by the confocal depth which for a given laser wavelength primarily depends on the numerical aperture (NA) of the microscope objective.

Surface-enhanced Raman spectroscopy (SERS) overcomes these restrictions including the light diffraction limitation by exciting surface plasmons in metallic nanostructures, that leads to the formation of intense local electromagnetic (EM) fields (hot spots) within a few nanometers from the SERS surface, allowing the investigation of chemical structures of the SLI. SERS is capable of detecting ultra-low concentrations of analyte, even at a single molecule level under optimized conditions. A major impediment towards wide use of this approach was the availability of high efficiency, stable SERS substrates. Roughened metal surfaces were first used as SERS substrates. However, these surfaces have a broad size distribution of hot spots, restricting experimental reproducibility and thus practical use of SERS. This problem was partially solved by shell-isolated nanoparticle-enhanced Raman spectroscopy (SHINERS). The major contribution to enhanced Raman intensity in SHINERS is from individual

nanoparticles (NPs), and SERS enhancement factors (EFs) are reported to be on the order of  $10^3.17$  By contrast, the EM field enhancement in the gap between NPs is greatly increased when two or more NPs are placed in close proximity to each other. The SERS EF of random silver NP aggregates is reported to be larger than  $10^7$ , approaching single-molecule sensitivity. However, the random NP aggregates lack long-range order and spatial homogeneity, leading to irreproducible SERS EF. 18, 19

We previously reported a strategy to self-assemble Au NPs into monolayers and deposit those monolayers onto arbitrary solid substrates. 18-20 The Au NPs in such monolayers had a hexagonal close packed (HCP) structure with controlled particle and gap dimensions. The resultant nanogap-SERS had an experimental EF up to 10<sup>7</sup> with mm<sup>2</sup>-scale spatial homogeneity.<sup>20</sup> The current study applies similar SERS substrate to probe spectroscopic signatures of solvent-salt interactions in lithium-ion battery electrolytes at the SLI. A new Fermi resonance (FR) Raman band was observed for the DEC carbonyl symmetric stretching band, which was not detected from standard Raman and FTIR spectroscopy measurements. Further, we estimate the solvation number, N, for LiPF<sub>6</sub> in EC-DEC solvent mixture to be close to 2 from gap-mode SERS for high salt concentration, while similar measurement for the same salt concentration from IR yields N >3. At low salt (LiPF<sub>6</sub>) concentration, both SERS and IR understandably show higher N with IR consistently showing higher coordination values. This discrepancy is likely due to the fact the solvation structures probed by SERS are confined by the SERS-active nano-gap regions and electrode surface whereas IR probes solvation structure in the bulk. Molecular dynamics (MD) simulations of the LiPF<sub>6</sub>/EC-DEC solvation structures indicate that the SERS nanogap dimensions) are comparable to the primary solvation shell which in principle could give a lower N compared to standard Raman and IR that can also detect secondary solvation shells. This work

demonstrates an approach for probing the ion solvation structures at varying length scales close to the interface (See SI last session) by manipulating the nanogap distance from the SERS substrate.

#### **Results and Discussion**

# I. SERS Analysis of Binary Solvent Mixtures and Salt

A semi-transparent pouch cell was used for the SERS study (Figure 1). The top high barrier (HB) film is transparent to the Raman laser (transmission is 92% at 785 nm, Figure S1), enabling vibrational spectroscopy of the electrolyte components on the SERS substrate. Details pertaining to the SERS cell fabrication and geometry are discussed in the supporting information.

Atomic force microscopy (AFM) of the Au NP monolayer film in Figure 2(a) gives a film thickness of 40.1 nm. This agrees with the average diameter of the NPs at 36.7 nm obtained from

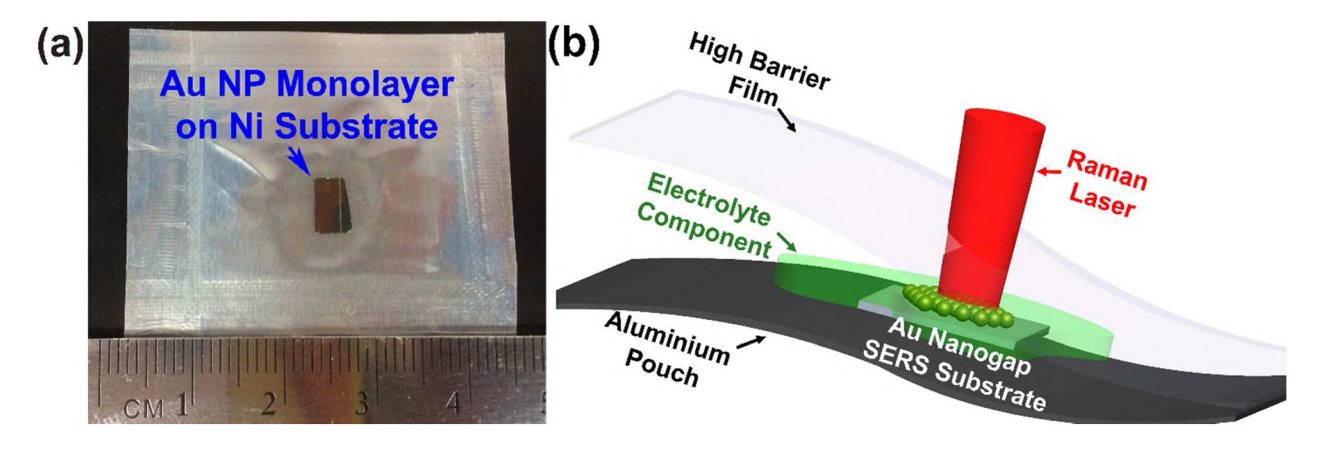


Figure 1. (a) Photograph of the semi-transparent pouch cell (top view). (b) Schematic illustration of the semi-transparent pouch cell (side view).

the TEM micrograph in Figure 2(b). The left inset of Figure 2(b) is a fast Fourier transform (FFT) of the TEM micrograph. It clearly indicates that the Au NPs are arranged in an HCP structure. The detailed structure of the interparticle gap is shown in the inset (right) of Figure 2(b), with average gap size  $1.6 \pm 0.5$  nm based on statistical analysis of over 700 Au NPs.  $^{21}$ 

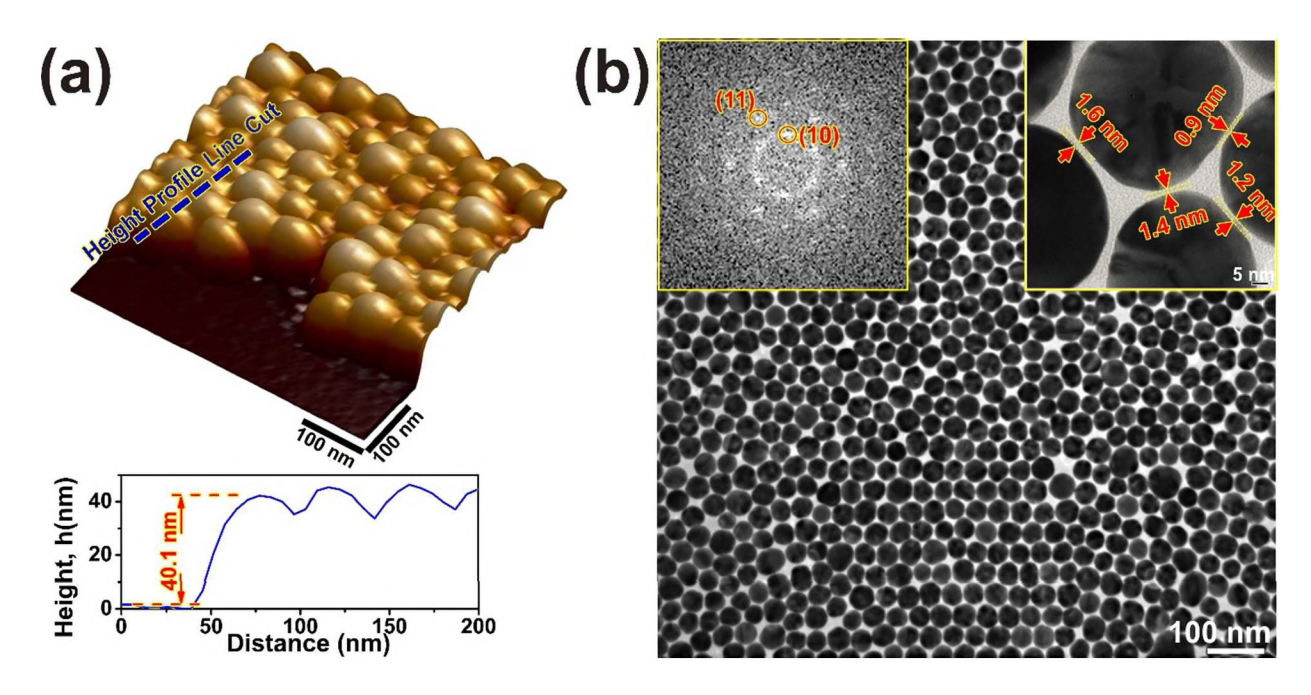


Figure 2. Characterization of the Au NP monolayers. (a) 3D AFM image taken at the film edge showing the NP film forms a monolayer on the Ni substrate. The height profile (bottom) corresponds to the line cut on the AFM image. The height of the film at the line cut is 40.1 nm, comparable with the average diameter of the NP at 36.7 nm. (b) TEM micrograph of the Au NP monolayers. Inset shows the FFT (left) and a magnified view of Au NP monolayers (right). The nanometer-gap between adjacent NPs is indicated by red arrows.

Commercial Li-ion batteries have a binary solvent electrolyte containing cyclic and linear carbonates. Here we use EC, DEC, and LiPF<sub>6</sub> as a model system to demonstrate the performance of the nanogap-SERS substrate. Both neat solvents and the electrolyte mixture show prominent SERS bands (Figure 3(a)). In sharp contrast, the signal from a standard Raman measurement under similar experimental condition (laser power, accumulation time and objective lens, *etc.*) appears as just background below the prominent SERS peaks as illustrated in Figure 3(a) and (c). It is worth mentioning that Raman spectroscopy has been used to study organic electrolyte components in the past, with typical laser power exceeding 10 mW<sup>22</sup> or even 50 mW<sup>23</sup> and signal integration times on the order of 100 seconds.<sup>23, 24</sup> The relatively high laser power and the extended laser exposure could potentially damage the analytes due to laser-induced heating. In

this study, the laser power was intentionally kept at low energy of less than 2 mW, with a total integration time of 10 s to reduce the heating effects. An attempt was also made to obtain a better signal-to-noise (S/N) ratio for the standard Raman spectra (Figure S2) by increasing the laser power up to 10 mW and extending the accumulation time to 300s. In contrast to conventional bulk Raman, the major fraction of Raman signal of the nanogap-SERS is from the analytes located within the nanogaps, where there is maximum field intensity.<sup>21</sup> The distance over which collective surface

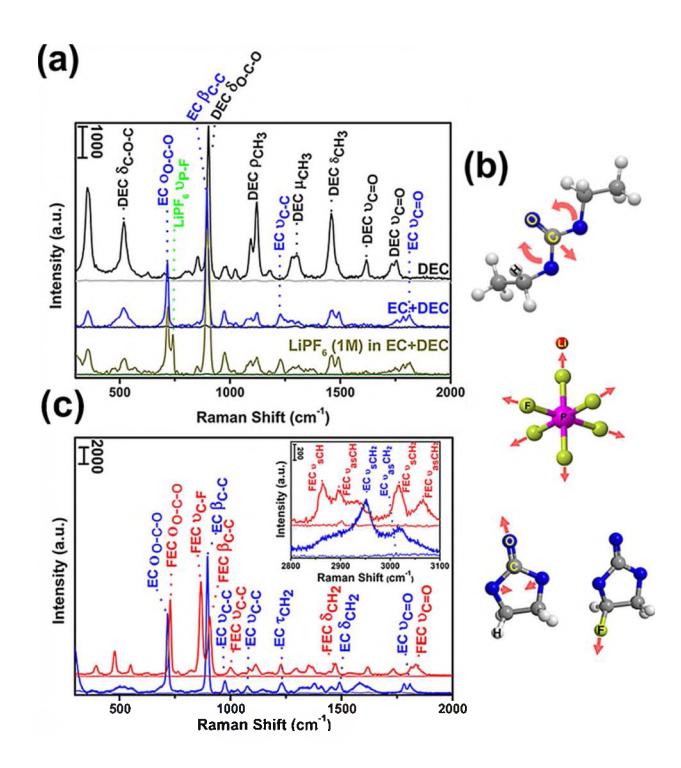


Figure 3. (a) SERS spectra of DEC, EC-DEC equivolume solution, and LiPF<sub>6</sub> (1M) in EC-DEC equivolume solution at room temperature and (b) Model molecular structures with vibrational modes indicated by red arrows. (top) Linear DEC molecule and  $\delta_{\text{O-C-O}}$  at 902 cm<sup>-1</sup>; (middle) LiPF<sub>6</sub> and symmetric  $v_{\text{P-F}}$  at 740 cm<sup>-1</sup>; (bottom left) EC molecule with ring breathing,  $o_{\text{O-C-O}}$  at 717 cm<sup>-1</sup> and (bottom right) FEC molecule with C-F symmetric stretching  $v_{\text{C-F}}$  at 868 cm<sup>-1</sup>. (c) SERS spectra EC and FEC at 39 °C on Au NP monolayer/Ni substrates. For both (a) and (c), standard Raman spectra were also collected from the same solvents and electrolytes for reference. These spectra, which are plotted below each SERS spectrum, are almost featureless for each sample. The Greek symbols denote corresponding vibrational modes for v, stretching;  $\delta$ , bending;  $\omega$ , wagging;  $\tau$ , twisting;  $\rho$ , rocking;  $\sigma$ , ring breathing and  $\sigma$ , ring deformation.

plasmon resonance (SPR) extends into media is reported to be less than 1 nm,<sup>25</sup> suggesting that nanogap-SERS is probing vibrational fingerprint of the analytes at a molecular scale.

As shown in Figure 3(a), the DEC SERS spectrum exhibits a prominent band at 902 cm<sup>-1</sup>, which was previously assigned to O-C-O bending  $(\delta_{\text{O-C-O}})^{26}$ . The chemical structure of DEC and the DEC  $\delta_{O-C-O}$  mode are schematically shown in Figure 3(b) top panel. The bands between 1050 cm<sup>-1</sup> and 1550 cm<sup>-1</sup> shown in Figure 3(a) are related to vibrations of DEC methyl groups. The intensity of 1122 cm<sup>-1</sup> band in this frequency range is insensitive to the chemical surroundings and can thus be used for spectral normalization (Figure S3).<sup>27</sup> The bands between 1650 and 1900 cm<sup>-1</sup> are assigned to the carbonyl group. These bands are known to be sensitive to the coordination of Li<sup>+</sup> cations. Seen in Figure 3(a) (also resort to Figure S5), the splitting of the DEC  $v_{C=0}$  band (around 1740 cm<sup>-1</sup>) stems from Fermi resonance (FR), in which an overtone or a combination vibrational mode appears by gaining spectral weight from a fundamental mode.<sup>28</sup> The FR resonance in this study may stem from the combination of the –OCO scissoring mode at 613 cm<sup>-1</sup> and the -CH<sub>3</sub> rocking mode at 1122 cm<sup>-1</sup> (Figure S6). An investigation on the physical origin of FR is beyond the scope of this work, but it may stem from local perturbation of DEC molecule at the local hotspot with an associated field gradient.<sup>2</sup> To our knowledge, this is the first observation of FR for DEC  $v_{C=0}$  band from a spectroscopic measurement.

Upon addition of EC to DEC (1:1 by volume), we observe a new band at 717 cm<sup>-1</sup> (Figure 3(a)), consistent with the combination of the EC ring breathing mode (EC  $o_{O-C-O}$ ) with an O-C-O symmetric stretching mode reported by Henderson *et al.*<sup>29</sup> Also, the DEC  $\delta_{C-O-C}$  band at 902 cm<sup>-1</sup> is overwhelmed by an EC band at 896 cm<sup>-1</sup>, assigned to EC skeletal deformation ( $\beta_{C-C}$ ) mode. The DEC carbonyl vibrational mode ( $v_{C-O}$ , doublet at 1735 and 1753 cm<sup>-1</sup>) decreases in intensity upon EC addition. A new doublet with maxima at 1785 and 1813 cm<sup>-1</sup> is assigned to EC  $v_{C-O}$ .

Upon solvation of LiPF<sub>6</sub> in the EC-DEC binary solvent, a new peak assigned to PF<sub>6</sub> symmetric stretching ( $v_{P-F}$ ) is observed at 740 cm<sup>-1</sup> (Figure 3(a)). This Raman peak partially overlaps with the EC o<sub>O-C-O</sub> band. (See Figure 3 caption for definition of symbols representing vibrational modes). Using the EC-DEC binary solvent as a model, the differences between the SERS and standard Raman spectra in terms of the frequency shift and line broadening are detailed in supporting information.

FEC is a common additive to form a stable SEI on high capacity anodes like silicon. 32 FEC has a similar chemical structure to EC, except that one hydrogen atom of a methylene bridge in the EC ring is replaced by a fluorine atom. To compare the SERS spectra of FEC and EC, the samples were heated to 39 °C, above the melting point of EC (T<sub>m</sub>= 34 °C). High intensity SERS bands from both species are observed, while the confocal Raman spectra are almost featureless (Figure 3(c)). In comparison to a single SERS peak at 896 cm<sup>-1</sup> for EC ( $\beta_{C-C}$ ), FEC shows two bands at this position. The 868 cm<sup>-1</sup> band is due to C-F stretching vibrations (v<sub>C-F</sub>), and the 908 cm<sup>-1</sup> band is due to FEC ring deformation (FEC  $\beta_{C-C}$  shown in Figure 3(c)). The lower vibrational frequency in the case of FEC is due to the heavy atom effect when F atom substitutes the H atom. Interestingly, some SERS bands are slightly shifted towards higher frequency for FEC compared with the counterparts in EC. The FEC  $o_{O-C-O}$  band is observed at 729 cm<sup>-1</sup>, which is 12 cm<sup>-1</sup> higher in frequency than the same band in EC. Additionally, the FEC skeletal stretching (FEC  $v_{C-C}$ ) at 1000 cm<sup>-1</sup> and 1088 cm<sup>-1</sup> are 25 cm<sup>-1</sup> and 12 cm<sup>-1</sup> higher in frequency than their EC counterparts, respectively. The carbonyl group stretching mode doublet  $(v_{C=O})$ shifts to 1814 cm<sup>-1</sup> and 1835 cm<sup>-1</sup> for FEC, compared to 1781 cm<sup>-1</sup> and 1807 cm<sup>-1</sup> for that of EC. EC shows two C-H stretching modes at 2952 cm<sup>-1</sup> and 3019 cm<sup>-1</sup>, whereas FEC exhibits four C-

H stretching bands at 2865 cm<sup>-1</sup>, 2898 cm<sup>-1</sup>, 3017 cm<sup>-1</sup> and 3066 cm<sup>-1</sup> (Figure 3(c) inset). This is due to the -CFH and -CH<sub>2</sub> asymmetric stretching in the FEC ring respectively.

To evaluate the performance of the gap-mode SERS quantitatively, the enhancement factor (EF) of various bands was calculated. As shown in Figure 4, the EFs collected from different bands range from  $10^3$  to  $10^5$ , with a maximum EF found for  $\beta_{\text{C-C}}$  at 897 cm<sup>-1</sup> in pure EC and  $\nu_{\text{C-F}}$  at 868 cm<sup>-1</sup> in FEC. The high EFs for neat EC and FEC could be due to their large dielectric constants, which promotes a larger SERS sensitivity. For example, at 25 °C, the permittivity of EC is 89.78, while the permittivity of DEC is only 2.8. The large EF for EC may stem from a stronger mutual interaction between the EC dipole moment and the EM-field in the nanogap compared to that for DEC.

Finite-difference time-domain (FDTD) simulations were used to evaluate the near-field EF

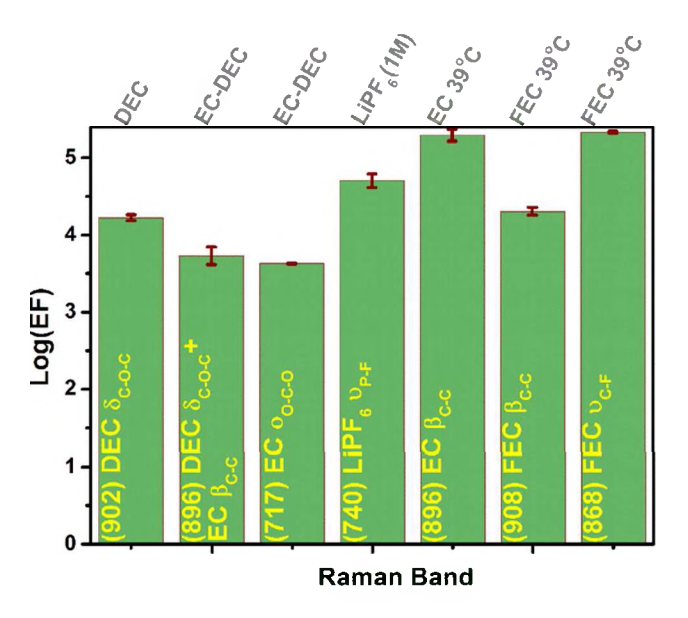


Figure 4. The calculated EF based on the integration of various bands of different species. The error bar represents the standard deviation based on at least five measurements at random locations of the same sample.

distribution on the nanogap SERS substrate. The model setup is shown in Figure S7. As the plane wave with the polarization direction, *E*, illuminates the Au NP monolayer surface (in the

xy-plane), the localized surface plasmons are excited. Due to the mutual constructive interference of the induced dipole moment of the surface plasmon, the most intense EM-field is localized in the nanogap between two adjacent Au NPs, with interparticle center-to-center axis parallel to E (Figure 5(a)).

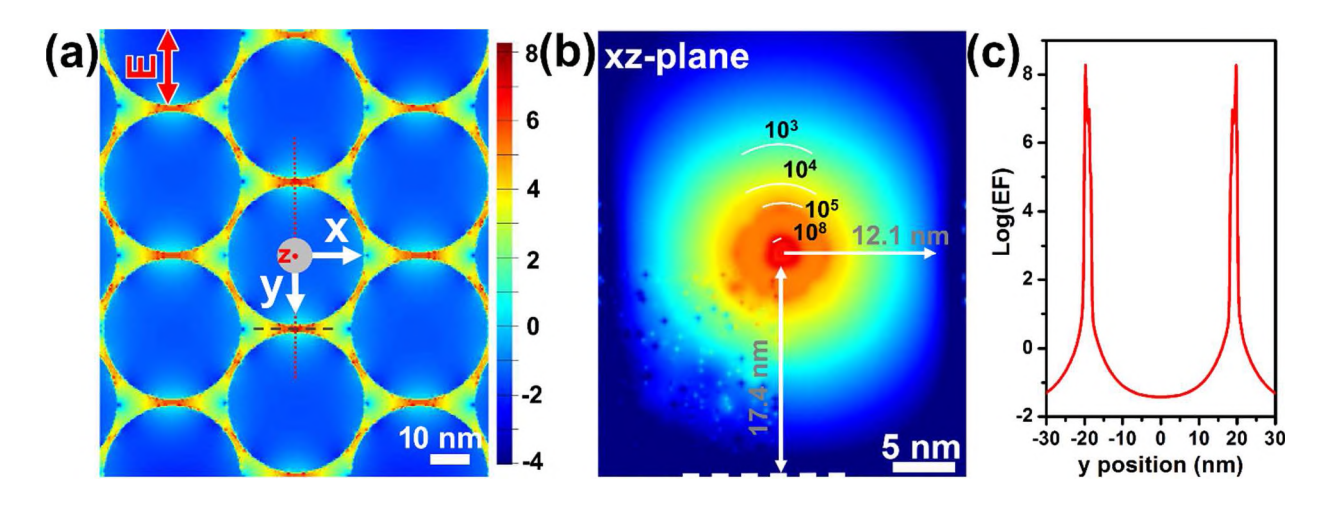


Figure 5. 3D FDTD simulation of HCP Au NP monolayer on Ni substrate. (a) The calculated enhancement factor distribution in an HCP unit cell in the xy-plane shown in logarithmic scale. The z axis (red dot) is normal to the xy-plane. The red arrow represents the polarization vector, **E**. The color bar represents the log(EF). (b) 2D log(EF) map in the xz-plane taken from the middle of the interparticle gap (black dashed line in (a)). The color bar is the same as that in (a). The maximum EF has a minimum distance of 17.4 nm to the Ni substrate (white dashed line). The center of the hot spot is 12.1 nm to the where log(EF) = 0. (c) Plot of the detailed EF distribution in an interparticle gap indicated by the red dashed line in (a). Each plot records the log(EF) across a horizontal line cut in the gap.

The EF distribution in a nanogap in the xz-plane is shown in Figure 5(b). The maximum EF value was found to be on the order of  $10^8$ , which is distributed close to the middle of the nanogap at  $x = \pm 0.9$  nm (where x = 0 for interparticle axis parallel to E). Out of this range, the EF rapidly decays to one at  $x = \pm 12.1$  nm, before reaching the nanoparticle in the adjacent superlattice direction. The total horizontal length (24.2 nm) of this region is smaller than the average NP diameter (36.7 nm) due to the hexagonal packing. The hot spot corresponding to the maximum

EF is located 17.4 nm from the solid substrate (Figure 5(b)), confirming that the vibrational information of the molecules was extracted from the immediate vicinity of the solid surface. The EF distribution across the y-axis (Figure 5(a)) over two nanogaps is detailed in Figure 5(c).

# II. LiPF<sub>6</sub> Salt Solvation in EC-DEC binary solvent mixture

The solution structure formed by addition of a lithium salt to binary carbonate solvent mixtures affects the electrolyte properties, such as ionic conductivity,<sup>34</sup> thermal and electrochemical stability,<sup>35</sup> and the formation of a stable SEL.<sup>36</sup> LiPF<sub>6</sub> at different molar concentrations in EC-DEC was used as a model electrolyte to understand the solvation structure (see Figure S8 for full SERS, Raman and IR spectra). It is worth mentioning that, standard Raman spectrum of each sample was collected at elevated laser power and extended collection time to increase the signal-to-noise (S/N) ratio (Figure S2). The intensity of the EC o<sub>O-C-O</sub> band in SERS (717 cm<sup>-1</sup>), Raman (720 cm<sup>-1</sup>) and IR (716 cm<sup>-1</sup>) spectra decreases with increasing salt concentration, whereas a new band at 729 cm<sup>-1</sup> (SERS and IR) and 733 cm<sup>-1</sup> (Raman) attributed to o<sub>O-C-O</sub> for EC coordinated with Li<sup>+</sup> cations gradually increases in intensity, (Figure 6(a)).<sup>29</sup>

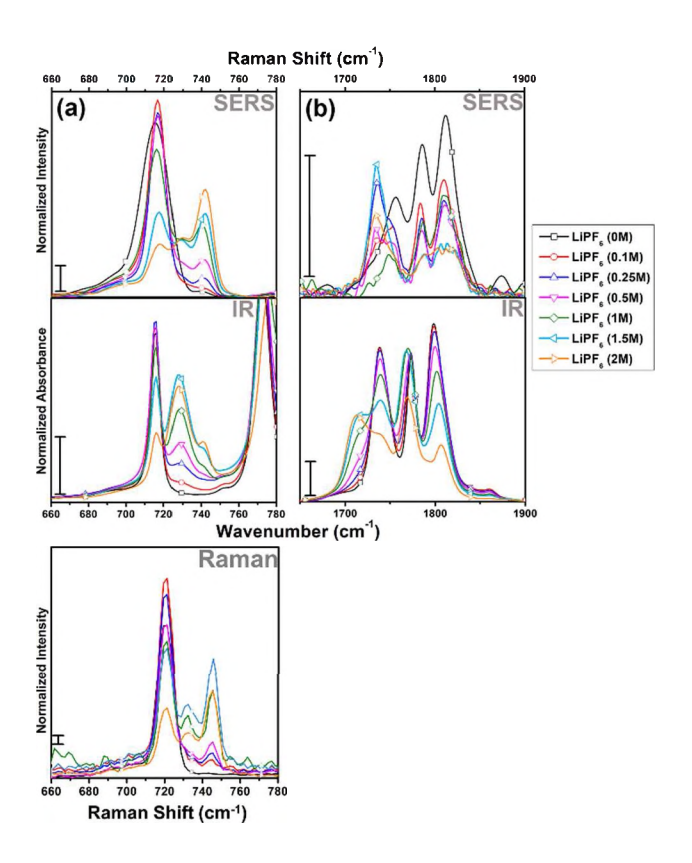


Figure 6. Comparison of SERS (top panel), IR spectra (middle panel) and standard Raman spectra (bottom) collected from solutions of various LiPF<sub>6</sub> molar concentrations. (a) Frequency region from 660 – 780 cm<sup>-1</sup> corresponds to EC ring breathing mode and PF6<sup>-</sup> P-F stretching mode. (b) Frequency region from 1650 – 1900 cm<sup>-1</sup> corresponds to the C=O stretching mode of EC and DEC. The scale bar represents 0.2 for all plots.

With increasing lithium molar fraction,  $X_{Li}$ , the band at ~740 cm<sup>-1</sup> (assigned to  $PF_6^-$  symmetric stretching ( $v_{P-F}$ )) increases in intensity (Figure S9).<sup>31</sup> The  $v_{P-F}$  band is prominent in SERS and Raman. However, in IR spectra the band appears as a small shoulder at the same frequency (Figure 6(a) middle) for all concentrations. The intense  $v_{P-F}$  mode in SERS allows for the determination of the band position (Figure S10). Trsic and co-workers<sup>31</sup> reported that for LiPF<sub>6</sub>/EC-DMC solution, the symmetric  $PF_6^-$  stretch,  $v_{P-F}$ , was observed at 739 cm<sup>-1</sup>, ascribed to solvent-separated ion pairs. They also showed that the band is blue-shifted to 745 cm<sup>-1</sup> in pure LiPF<sub>6</sub> salt. We observed a similar trend, where the  $PF_6^ v_{P-F}$  band centers at 740 cm<sup>-1</sup> for  $X_{Li} \le$ 

2.2%, and gradually blue-shifts to 742 cm $^{-1}$  with increasing  $X_{Li}$ . This also suggests that contact ion pairs are formed at high salt concentration. <sup>37</sup>

Peak deconvolution in this frequency region allows for quantitative analysis of the EC-Li $^+$  coordination based on the o<sub>O-C-O</sub> band (supporting information "SERS and IR band deconvolution"). The ratio of the solvated EC band to the unsolvated band (R<sub>EC S</sub>) was calculated as:

$$R_{ECS} = \frac{A_s}{A_s + A_u} \tag{1}$$

where  $A_s$  and  $A_u$  are the integrated bands of coordinated EC o<sub>O-C-O</sub> and uncoordinated EC o<sub>O-C-O</sub>, respectively. An empirical 2<sup>nd</sup> order polynomial best describes the dependence of R<sub>EC S</sub> on X<sub>Li</sub> (Figure 7(a)).

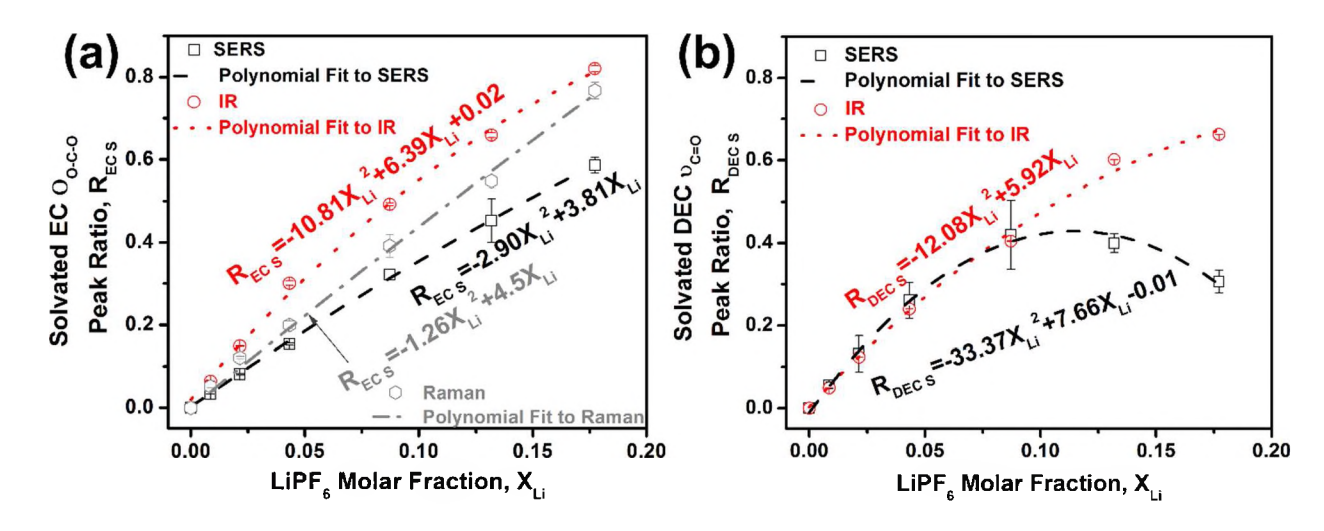


Figure 7. Regression curves correlating the lithium salt solvation-related peak ratio to LiPF<sub>6</sub> molar percentage for SERS, Raman and IR. (a) Variation in the ratio of solvated EC ring deformation ( $O_{O-C-O}$ , 729 cm<sup>-1</sup>) over the sum of unsolvated EC Oo-c-o (717 cm<sup>-1</sup>) and solvated EC  $O_{O-C-O}$  with the LiPF<sub>6</sub> mole fraction,  $X_{Li}$ . (b) The plot of the ratio of the solvated DEC  $v_{C=O}$  peak integration to the sum of solvated and unsolvated peak integration of DEC  $v_{C=O}$  versus  $X_{Li}$ .  $R^2 \ge 0.99$  for all fittings.

Obtaining meaningful solvation number for EC and DEC with Li $^+$  cations from EC ring breathing ( $\beta_{\text{C-C}}$ , 896 cm $^{-1}$ ) and DEC O-C-O bending ( $\delta_{\text{O-C-O}}$ , 902 cm $^{-1}$ ) peaks is difficult due to the overlap of coordinated and uncoordinated EC and DEC carbonyl bands (Figure S11). We use IR spectra in this frequency region to gain complementary information for the solvation structure of DEC-Li $^+$  and EC-Li $^+$ . As  $X_{\text{Li}}$  increases above 8.7%, a band at 836 cm $^{-1}$  becomes prominent, consistent with the formation of the contact ion pairs or aggregates in solution of LiPF<sub>6</sub> in EC-DMC .<sup>37</sup>

The EC and DEC carbonyl band position and intensity (Figure 6(b)) are sensitive to the local chemical environment, which change upon coordination with Li<sup>+37</sup> The intensity of EC  $v_{C=0}$ (1785 cm<sup>-1</sup> and 1813 cm<sup>-1</sup> for SERS and 1773 cm<sup>-1</sup> and 1800 cm<sup>-1</sup> for IR) decreases with increasing X<sub>Li</sub> due to the decrease of uncoordinated EC upon Li<sup>+</sup> coordination to the EC carbonyl group.<sup>37</sup> Interestingly, for  $X_{Li} \ge 13.2\%$ , the SERS EC  $v_{C=O}$  doublet turns into a shoulder, while the doublet structure remains in the IR spectra (Figure 7(b)). The reason might be that the coordinated EC  $v_{C=O}$  of the contact ion pair formed at high salt concentration has low Raman polarizability in the nanogap. Unfortunately, the DEC carbonyl stretching mode at this frequency region has an unsatisfying S/N ratio. Thus, it was difficult to perform a meaningful quantitative analysis (Figure S2(c) and (d)) in this frequency region. For both SERS and IR, the  $v_{C=O}$  doublet of coordinated EC overlaps with that of uncoordinated EC, preventing meaningful band deconvolution.  $^{30, 37, 38}$  With increasing LiPF<sub>6</sub> concentration, the SERS DEC  $\nu_{C=O}$  band at 1753 cm<sup>-1</sup> and the FR band at 1735 cm<sup>-1</sup> decrease in intensity, whereas two new bands at 1744 cm<sup>-1</sup> and 1725 cm<sup>-1</sup> gain in intensity accordingly (see Figure S12(c) for peak deconvolution). The latter two bands are a result of the DEC carbonyl coordination to Li<sup>+</sup>, and are not reported before to our knowledge. In IR, the uncoordinated DEC  $v_{C=O}$  band at 1740 cm<sup>-1</sup> decreases in intensity

with increasing  $X_{Li}$ , while the coordinated DEC  $v_{C=O}$  band intensity at 1715 cm<sup>-1</sup> gradually increases (see Figure S12(d) for peak deconvolution). Quantitative analysis of the ratio of coordinated to uncoordinated DEC  $v_{C=O}$  band,  $R_{DEC\ S}$  is shown in Figure 7(b). While this ratio can be fit to a 2<sup>nd</sup> order polynomial (based on SERS and IR experiments), clearly there is a maximum  $R_{DEC\ S}$  value for 8.7% <  $X_{Li}$  < 13.2% for SERS. The existence of the maximum point in SERS  $R_{DEC\ S}$  –  $X_{Li}$  plot might stem from the competition between the increasing number of coordinated DEC carbonyl groups and the decreasing Raman cross section of the DEC carbonyl stretch.<sup>34</sup>

The average solvation number, N, of EC or DEC coordinated to Li<sup>+</sup> cation can be estimated from the following set of equations:  $^{37,39,40}$ 

$$C_{s} = NC_{Li}$$

$$C_{s} = \frac{A_{s} / a}{A_{s} / a + A_{u}} C_{o}$$

$$N = \frac{A_{s} / a}{A_{s} / a + A_{u}} \frac{C_{o}}{C_{Li}}$$
(2)

where  $C_s$ ,  $C_o$ , and  $C_{Li}$  are the molar concentrations of the Li<sup>+</sup>-coordinated solvent, total solvent, and LiPF<sub>6</sub>, respectively. The constant a is a scaling factor. Several similar studies assumed the coordinated solvent molecule had the same Raman scattering/IR absorption coefficients as the uncoordinated solvent molecule (a=1). <sup>37, 39</sup> By taking into account the implicit and explicit interactions of the solvent molecules in DFT analysis, Henderson *et al.* found that the vibrational modes (*e.g.* EC C=O vibration) tended to have underestimated Raman activity upon Li<sup>+</sup> coordination, and strong disagreement occurred among solvation numbers calculated from different vibrational modes. <sup>29</sup> On the other hand, the coordinated C=O vibration of the propylene carbonate (PC) was found to gain intensity by 7-16%, and up to 60% for coordinated dimethyl carbonate (DMC) C=O band intensity, as indicated by cluster-continuum DFT

calculations for IR. <sup>40</sup> For the case of the ion solvation in a binary electrolyte (LiPF<sub>6</sub> in EC-DMC), Borodin *et al.* found that the discrepancies among the solvation numbers obtained from Raman and IR experiments could be reconciled by scaling the intensity of coordinated bands. <sup>41</sup> In the current study, the solvation information for DEC from the standard Raman spectra was missing due to the low S/N ratio in the carbonyl frequency region (Figure S2). To directly compare the solvation numbers obtained by SERS, IR, and those in other studies, a proper evaluation of the scaling factor for related vibrational bands for each solvent is needed.

It was reported that the EC<sub>3</sub>/Li<sup>+</sup> complex (3 EC molecules surrounding a Li<sup>+</sup>) reasonably represents the influence of Li<sup>+</sup> coordination to EC on the Raman spectra, with an estimated scaling factor of 0.88 for the ca. 738 cm<sup>-1</sup> Raman band (corresponding to coordinated EC) to accurately determine the Li<sup>+</sup>-solvent solvation interactions. <sup>29</sup> Here we assume the same value for coordinated EC spectra in both Raman and SERS (a = 0.88). Note that for a LiPF<sub>6</sub>-EC-DMC system, the DMC Raman activity remained almost the same upon Li<sup>+</sup> coordination. We thus assume a = 1 for DEC in the LiPF<sub>6</sub>-EC-DEC system, since lithium salts have similar solvation and dissociation properties in DEC and DMC solutions. <sup>42</sup> In a related solution structure study for the LiPF<sub>6</sub>-PC-DMC system, the maximum scaling factor for the C=O IR band for coordinated PC was reported to be 1.16, depending on the DFT calculations. <sup>40</sup> The same scaling factor was between 1.3 and 1.64 for DMC. Therefore, to account for the maximum influence of the Li<sup>+</sup> coordination to EC and DEC on the related IR bands, we use a = 1.16 for EC, and 1.3 and 1.64 (maximum scaling factor) for DEC. The calculated salvation numbers in conjunction with those reported by other closely related studies were summarized in Figure 8(a) and (b).

An immediate observation from Figure 8(a) is the good agreement between the scaled EC solvation number from IR and Raman (difference < 0.3 for all LiPF<sub>6</sub> molar fractions), two bulk

spectroscopy techniques. This indicates that the scaling factor estimated here is accurate to the first decimal place, comparable with a similar study on a LiPF<sub>6</sub>-EC-DMC electrolyte. <sup>41</sup>  $N_{EC}$  calculated by SERS is smaller than its counter parts measured with Raman and IR, which is indicative of a different coordination behavior of EC to  $Li^+$  at the direct SLI than in bulk electrolyte. Interestingly,  $N_{DEC}$  measured by SERS is slightly higher than that by IR when  $X_{Li} < 10.9\%$ . while the latter outperforms the former  $X_{Li} > 10.9\%$ , This indicates that at lower  $Li^+$  concentration, more DEC molecules surround the  $Li^+$  at the SLI than in bulk electrolyte. However, when  $X_{Li} > 10.9\%$   $N_{DEC}$  from IR is greater than  $N_{DEC}$  from SERS. For both IR and SERS measurements,  $N_{EC}$  is higher than  $N_{DEC}$  at each  $LiPF_6$  molar fraction, although the molar ratio of DEC to EC is 1:0.55 for an EC-DEC equivolume solvent. This is in accordance with similar investigations on the EC- $Li^+$  solvation at the graphite anode surface by mass spectrometry <sup>43</sup> and in EC-DMC by <sup>17</sup>O NMR. <sup>44</sup> Another major factor could be due to the much higher permittivity of EC (32 times that of DEC) making it much more polarizable.

The comparison between the total solvation number, N(Total) obtained from SERS and IR is shown in Figure 8(b). It is clear that the total solvation number obtained from SERS is smaller than that from the IR, even if the maximum scaling factor (a = 1.64) was used to account for the intensity increase of the coordinated DEC carbonyl group for IR. The difference between  $N_{SERS}$  and  $N_{IR}$  is about 1, suggesting that on average the solvation shell probed by SERS at the SLE has 1 less solvent molecule than that probed by IR from the bulk electrolyte. It is generally accepted that tetra-coordination (N = 4) best describes the complex of aprotic solvents and  $Li^+$  in the primary solvation shell at low lithium salt concentration. <sup>37, 39</sup> From SERS, the total solvation number of EC and DEC is larger than 4 for less concentrated electrolyte ( $X_{Li} < 8.7\%$ ), most likely resulting from the secondary solvation shell in the nanogap region. <sup>45</sup> N(Total) decreases

with increasing  $X_{Li}$ , due to the decreasing total number of solvent molecules per  $Li^+$  at larger salt concentration. For  $X_{Li} = 8.7\%$ ,  $N_{tot}$  drops below 4.2 to 3.4. However, as N(Total) is quite close to 4, the dominating solution structure is still solvent separated ion pairs (SSIP). Further increasing  $X_{Li}$  to 13.2% and 17.7% results in N(Total) decreasing to 2.8 and 2.3, respectively. This suggests at least one carbonate molecule has been replaced by a PF anion in the solvation shell in which the contact ion pairs (CIP) or aggregates predominate. This is in good agreement with the above solvation structure analysis based on SERS EC  $v_{C=O}$  and IR  $v_{P-F}$  (Figure S11). We compared our solvation number results with similar studies (Figure 8(b)). Noticeably, the solvation number reported for LiPF<sub>6</sub> in PC using corrected IR carbonyl band intensities, <sup>40</sup> and for LiPF<sub>6</sub> in EC using corrected Raman C=O band activities 29 were all slightly higher than that acquired from SERS in the current study. The solvation number of the LiPF<sub>6</sub> in PC-DEC, DEC and PC systems calculated by uncorrected IR absorbance <sup>37</sup> are higher than those obtained by using scaling factors, emphasizing the necessity of using the scaling factors in the solvation number analysis. Overall, the solvation trend obtained by SERS result agrees reasonably well with that by IR and other studies, but SERS reflects a smaller solvation number at SLI at each LiPF<sub>6</sub> concentration compared to the results from the bulk spectroscopy techniques.

The competitive solvation of  $\operatorname{Li}^+$  by DEC EC molecules is reflected by the solvation number of each carbonate solvent ( $N_{DEC}$  and  $N_{EC}$ ). To get further insight into the discrepancies between the solvation number obtained from the SLI by SERS and that from the bulk by IR, we performed gas phase MD simulations. From the MD simulations we obtained the relative binding energy of the carbonate to  $\operatorname{Li}^+$  and the solvation shell dimensions for different numbers of solvent molecules surrounding a  $\operatorname{Li}^+$ . For more accurate quantum chemistry simulations that

depict the competitive Li<sup>+</sup> solvation between linear and cyclic carbonate electrolytes in a condensed phase, readers may refer to work from Chapman *et al.* and Borodin *et al.* <sup>40, 41</sup>

Figure 8(c) shows the MD simulation of different bonding environments from a total EC coordination to total DEC coordination to a Li<sup>+</sup> cation. The binding energies and relative stabilities are discussed in the supporting information. In summary, the magnitude of the absolute binding

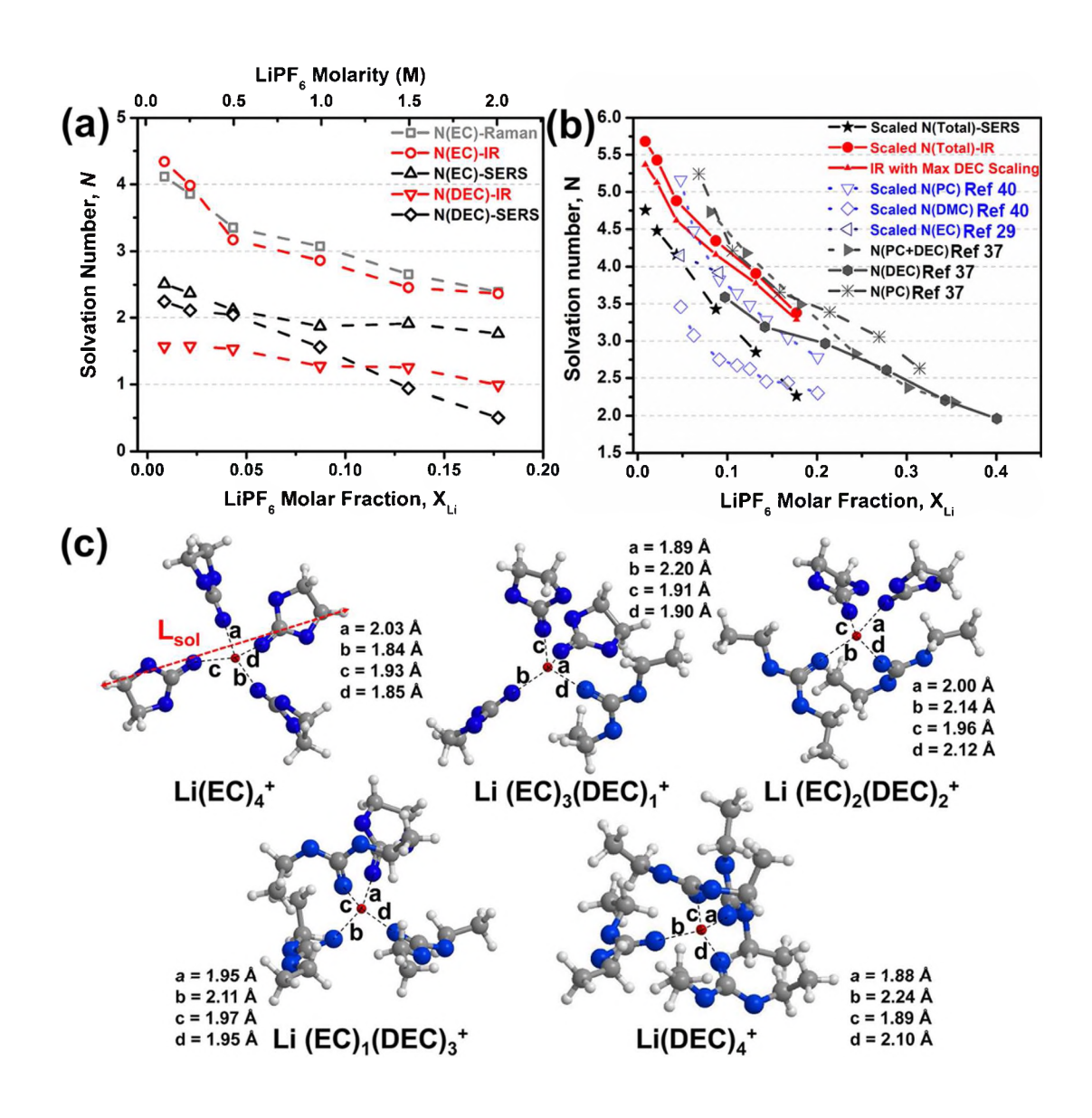


Figure 8. Calculated solvation number from (a) SERS and (b) IR spectra with changing mole fraction of LiPF<sub>6</sub> in EC-DEC binary solvent. N was calculated for EC based on EC ring deformation ( $O_{O-C-O}$ ), and for DEC based on DEC C=O stretching ( $v_{C=O}$ ). (c) Optimized structures of the primary solvation shell formed by the carbonyl group of EC and/or DEC coordinating to Li<sup>+</sup>. The spheres in blue, grey, white, and red represents "O", "C", "H" and "Li<sup>+</sup>" atoms, respectively. The values of a,b,c, and d represents the Li<sup>+</sup>…O bond length for the corresponding Li<sup>+</sup>-solvent complex.

energy of  $\text{Li}(\text{EC})_4^+$  is highest, indicating its formation is the most favorable among the five  $\text{Li}(\text{solvents})_4^+$  complexes. The replacement of an EC by a DEC molecule comes with an energy penalty of 1.4 kcal mol<sup>-1</sup>. For comparison, the enthalpy penalty for replacing an EC molecule in the  $\text{Li}(\text{EC})_4^+$  complex by a DMC molecule is about 2.3 kcal mol<sup>-1</sup> based on DFT calculations.<sup>37</sup> The observation that  $\text{Li}(\text{EC})_4^+$  is the most favorable structure agrees fairly well with similar DFT studies on aprotic liquid electrolytes. <sup>46</sup> The formation of  $\text{Li}(\text{EC})_4^+$  is ~10 kcal mol<sup>-1</sup> more favorable than that of  $\text{Li}(\text{EC})_2(\text{DEC})_2^+$  and  $\text{Li}(\text{EC})_1(\text{DEC})_3^+$ , in accordance with the previously reported value of 17 kcal mol<sup>-1</sup>. <sup>47</sup> The least favorable tetrahedral solvation structure,  $\text{Li}(\text{DEC})_4^+$ , has 27.8 kcal mol<sup>-1</sup> lower binding energy than that of  $\text{Li}(\text{EC})_4^+$ .

For SERS, at lower salt concentrations ( $X_{Li} < 8.7\%$ ), the difference between  $N_{DEC}$  and  $N_{EC}$  is small (< 0.27). This difference increases to 0.3 at  $X_{Li} = 8.7\%$ , to 0.97 at  $X_{Li} = 13.2\%$ , and to 1.26 at  $X_{Li} = 17.7\%$ .  $N_{EC}$  value slightly decreases to around 1.8 at X = 17.7% from 2.1 at  $X_{Li} = 4.3\%$ . This clearly indicates that the  $PF_6^-$  anion would preferably replace DEC rather than EC with increasing salt concentration. Our results are in agreement with modeling by Sankaranarayanan and co-workers, in which the absolute binding energy of the  $Li(EC)_4^+$  complex was 37 kcal mol<sup>-1</sup> greater than  $Li(DEC)_4^{+}$ .

The solvation number calculated from IR is noticeably larger than that derived from SERS, especially at low LiPF<sub>6</sub> concentrations ( $X_{Li} < 4.3\%$ ), N(Total)-IR>5>N(Total)-SERS. Clearly, the IR signal is not restricted by the spatial confinement of nanogap SERS (Figure S13) and is

therefore sensitive to the carbonate solvents bound to the second solvation shell, assuming the tetrahedral solvation structure in the primary solvation shell persists. However, at low salt concentration (X<sub>Li</sub> < 10.9%), IR N<sub>DEC</sub> is smaller than SERS N<sub>DEC</sub>, with the maximum difference (~1) at the lowest salt concentration. N<sub>EC</sub> measured by IR or Raman is larger than that of SERS by almost 2, suggesting that the major contribution to the second solvation sphere in bulk electrolyte is from EC. Lucht et al. 37 studied the solvation structure of LiPF<sub>6</sub> in PC and DMC using FTIR-ATR. The average solvation numbers were ~5 for PC and DMC in 0.8 M LiPF<sub>6</sub>. In this study, the IR  $N_{tot}$  is 5.6 at  $X_{Li} = 4.3\%$  (0.5 M LiPF<sub>6</sub>), which agrees well with the results of Lucht et al., given that the dielectric constants of PC and DMC are close to those of EC and DEC, respectively. 48 However, the lowest Li<sup>+</sup> concentration was 0.8 M in their report, so that results at lower salt concentrations cannot be compared. According to a recent study by Xu and co-workers, 44 the maximum solvation number of EC surrounding a Li<sup>+</sup> ion was 6 in both primary and secondary solvation shells for LiPF<sub>6</sub> (1M) in EC-DMC equivolume solution. Therefore, it is reasonable that  $N_{tot} = 5.68$  and 5.42 at the two lowest LiPF<sub>6</sub> concentrations (0.1M and 0.25M) in this study. It is important to consider if the solvation structure could be altered by the high local EM-fields necessary for SERS. We estimate that the maximum electric fields generated in our SERS experiment are at least two orders of magnitude too low to alter the solvation structure formed by Li<sup>+</sup> and carbonate solvents. Details of this calculation can be found in the supporting information. However, the Raman scattering tensor for a given vibrational mode of a probed molecule is dictated by the orientation of the molecule with respect to the local EM vector field. <sup>49</sup> Since molecular orientation determines the Raman scattering intensity, reorientation of the solvation shells within the nanogap may influence the SERS intensity.

## III. PCA and MCR Analysis of SERS and IR

The previous section discusses the variation of solvation number (N) with salt concentration based on the SERS and IR spectral. More quantitative analysis on different solvation regimes with differing salt concentration can be obtained from principal component analysis (PCA) and multivariate curve resolution (MCR) analysis of the Raman and IR spectra. <sup>50</sup> In this context, we carried out PCA and MCR analysis of SERS, standard Raman spectra, and IR spectra with varying LiPF<sub>6</sub> concentrations in EC-DEC binary solvent. PCA determines the minimum number of spectral components needed in linear combination to obtain the sample spectra variation. The pure component spectra were then extracted by MCR using alternating least-squares curve fitting (see SI for details). Two spectral components were found in LiPF<sub>6</sub>/EC-DEC system, with the first one attributed to the solvent separated ion pair (SSIP) in EC-DEC binary solvent, and the second one related to the contact ion pair (CIP) or aggregates (Figure S14). SERS, standard Raman spectra and IR spectra indicate that the SSIP spectra component decreases with increasing X<sub>Li</sub>, whereas the CIP or ion aggregates increases versus X<sub>Li</sub> (Figure 9). This is in agreement with the solution structure change observed in Figure 6. Interestingly, the SERS component molar fraction of SSIP drops sharply when  $X_{Li} > 8.7\%$ , until CIP starts dominating at  $X_{Li} = 13.2\%$  (Figure 9), in agreement with the coordination number analysis for SERS (Figure 8(a)). However, the PCA-MCR analysis for bulk electrolyte as reflected by Raman and IR indicates that CIP already prevails over SSIP at  $X_{Li} = 8.7\%$ . Note that the total solvation number,  $N_{tot}$  is larger than 4 for IR at  $X_{Li} = 8.7\%$ 

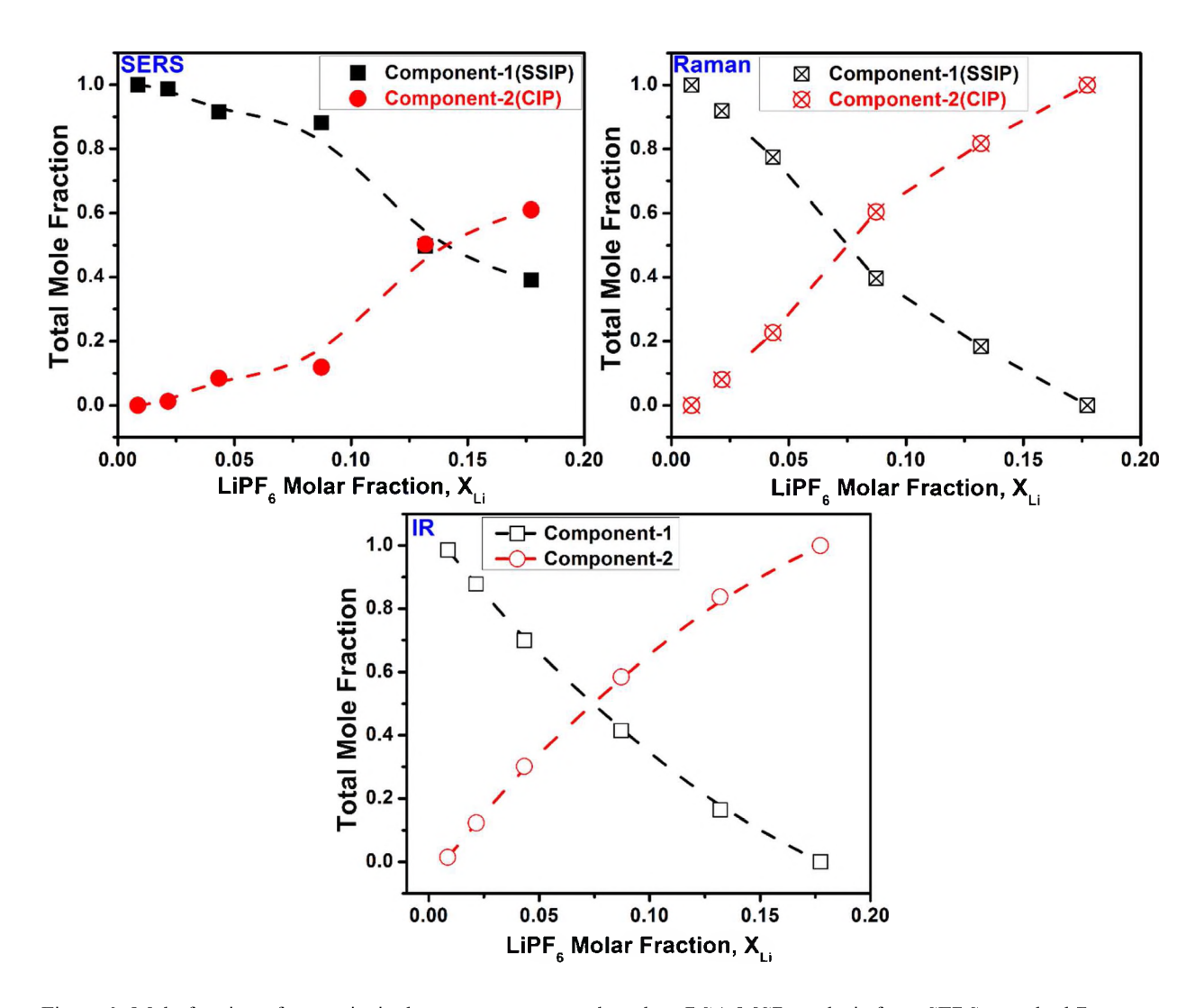


Figure 9. Mole fraction of two principal component spectra based on PCA-MCR analysis from SERS, standard Raman spectra and IR spectra with changing molar fraction of LiPF<sub>6</sub> in EC-DEC binary solvent.

(Figure 8(b)). This suggests that in about 60% of the primary solvation shells, at least one carbonate solvent molecule is substituted by a  $PF_6^-$  anion with CIP formation, and more than one carbonate molecule is present in the second solvation shell. Such a secondary solvation shell structure is not detected by nanogap SERS at  $X_{Li} = 8.7\%$ , possibly due to the larger dimension of the secondary solvation shell compared to the average nanogap size of 1.6 nm. It is worth noting that, when using the monolayer Au NP SERS substrate to probe the solvation structure directly at the SLI in a Li-ion battery, the case could be more complicated (Figure S16). In addition, it has been shown that the solvation structure of Li<sup>+</sup>-carbonates differs with respect to the electrode

potential at the SLI. <sup>51</sup> It should be interesting to evaluate the solvation structure evolution at the SLI with different bias potentials applied to the electrode. The related study is currently ongoing in our lab.

#### **Conclusions**

Understanding of the ion solvation (and desolvation) of electrolytes at the solid electrode/liquid electrolyte interface is critical to stabilize interfaces for better Li-ion battery performance. The Au nanogap SERS substrates developed here enables the acquisition of the spectroscopic signatures of electrolyte solvation immediately adjacent to the solid surface containing hotspots. The gap-mode SERS is capable of probing new vibrational modes (*e.g.* Fermi resonance) of electrolyte species with much higher degree of sensitivity compared to micro-Raman. Detailed analysis on the solvation-related SERS bands indicates that competitive solvation exists between EC/Li<sup>+</sup> and DEC/Li<sup>+</sup> at the SLI. The relative dimensions of various Li(solvent)<sub>n</sub><sup>+</sup> complexes within the nanogaps reflects that SERS favors the characterization of the tetra-coordination of the primary solvation shell, which is in agreement with modeling studies reported earlier. Solvation number obtained from standard Raman and IR analysis reports larger values as they could be sensitive to Li coordination beyond the primary solvating shell.

The concept of nanogap-SERS built upon Au NPs monolayers is potentially capable of providing a fast, noninvasive, and highly-sensitive characterization tool for probing fundamental properties of the SLI, which constitute an essential step towards a better understanding of the SLI solution structures in broad applications such as water desalination, catalysis, corrosion, energy storage and ion distribution/transport through biological membranes, *etc*.

#### Methods

Ti and Ni sputtering targets (both 99.995% pure) were purchased from Kurt J. Lesker. Transparent high barrier (HB) film (ScotchpakTM HB428) coated with a heat sealable ethylene vinyl acetate copolymer and a ceramic oxide particle layer was generously supplied by 3M. Ethylene carbonate (EC, anhydrous, ≥ 99%), diethyl carbonate (DEC, anhydrous, ≥ 99%), fluoroethylene carbonate (FEC), and lithium hexafluorophosphate (LiPF6, battery grade) were purchased from BASF. Aluminum laminated film (EQ-alf-400-7.5M) was purchased from MTI All materials were used as received.

Ni substrate fabrication

A Ni current collector with a Ti adhesion layer was coated on a quartz substrate *via* DC magnetron sputtering in Ar plasma. Sputtering of both metals was conducted at 10 W power, 20 mTorr pressure with a 5 cm throw distance, resulting in a deposition rate of about 0.5 and 1.9 nm s<sup>-1</sup> and total thicknesses of 2 and 100 nm for Ti and Ni, respectively.

Au NP synthesis and self-assembly

Aqueous colloidal gold nanoparticles of average diameter  $36.7 \pm 2.8$  nm were synthesized using a "seed-growth" method detailed in a previous study.<sup>21</sup> A three-phase self-assembly technique was used to fabricate Au NP monolayers on the nickel substrates.<sup>19</sup>

Transparent Raman cell fabrication

HB film and laminated aluminum pouch material were precut into 3.5 cm  $\times$  4.5 cm rectangular sheets. The Au monolayer on Ni substrate and 200  $\mu$ L of each solvent or electrolyte sample were sandwiched between the HB film and Al pouch and sealed by an impulse heat sealer (AIE200) in an Ar-filled glovebox (both O<sub>2</sub> and H<sub>2</sub>O < 0.1 ppm). A series of LiPF<sub>6</sub> in EC-DEC equivolume solutions were made in an Ar-filled glove box. The molar concentrations of LiPF<sub>6</sub> in EC-DEC

solution were 0 M, 0.1 M, 0.25 M, 0.5 M, 1 M, 1.5 M, and 2 M (LiPF<sub>6</sub> molar fraction,  $X_{Li} = 0$ , 0.9%, 2.2%, 4.3%, 8.7%, 13.2% and 17.7%, respectively).

#### Characterization

The Au NP monolayers were deposited on glass slides for ultraviolet-visible-near infrared (UV-vis-NIR, Cary 5000) spectroscopy, on Ni wafers for atomic force microscopy (AFM, Bruker, MultiMode 8) and for Raman spectroscopy (inVia Renishaw, 785 nm local power < 2mW, exposure time = 10 s, number of scans = 1 and grating = 1200 grooves/mm, 50x objective, N.A. = 0.75 and depth resolution  $\approx 2~\mu m$ ) and on carbon-coated copper grids for transmission electron microscopy (TEM, JEOL 2011). IR spectra of each sample were collected from a Fourier Transform Infrared (FTIR) spectrometer (Bruker, ALPHA) with a diamond attenuated total reflection (ATR) accessory. Spectra were collected in the region from 4000 to 650 cm<sup>-1</sup> with 128 scans and 2 cm<sup>-1</sup> resolution. The IR measurements were performed in an Ar-filled glove box with  $O_2$  and  $O_2$  and  $O_3$  ppm.

# Simulations

Three-dimensional (3D) finite-difference time-domain (FDTD) simulations were used to study the EM field distribution in the Au NP monolayer, similar to what has been reported previously.<sup>21</sup> The spatial mesh size was 0.25 nm. Molecular dynamics (MD) simulations were run using MMFF94 force field<sup>52</sup> through the ChemBio 3D Ultra 12.0 software package. Details can be found in supporting information.

#### ASSOCIATED CONTENT

The authors declare no competing financial interest.

#### **AUTHOR INFORMATION**

# **Corresponding Author**

- \* Corresponding Author
- \*nandaj@ornl.gov
- \*dhallinan@fsu.edu

## **ORCID**

Jagjit Nanda: 0000-0002-6875-0057

Guang Yang: 0000-0003-0583-6272

#### **Author Contributions**

JN, GY, DH conceived the idea and designed the experiments. GY, II, VS performed the experiments. GY performed the simulations. All authors contributed to data analysis and to the manuscript draft and editing. All authors have given approval to the final version of the manuscript.

## ACKNOWLEDGMENT

This research conducted at Oak Ridge National Laboratory, managed by UT Battelle, LLC, for the U.S. Department of Energy (DOE) under contract DE-AC05-00OR22725 is supported by the Office of Energy Efficiency and Renewable Energy (EERE) Vehicle Technologies Office (VTO). SERS measurements were performed at the Center for Nanophase Materials Sciences, which is a DOE Office of Science User Facility. RLS acknowledges support from the Fluid

Interface Reactions Structures and Transport (FIRST) Center, an Energy Frontier Research Center funded by the U.S. Department of Energy, Officer of Science, Office of Basic Sciences. VS thanks European Union's Horizon 2020 research and innovation program under the Marie Sklodowska-Curie grant agreement No. 690898. DH thanks the start-up funding supplied by the Florida State University and the FAMU-FSU College of Engineering. The authors are in debt to Drs. Nancy J. Dudney, Gabriel M. Veith, Andrew K. Kercher for fruitful discussions.

# **Supporting Information**

Supporting Information Available: < Transmittance curve of the HB film, schematic of the 3D FDTD simulation, SERS and IR spectral overview of the LiPF<sub>6</sub> in EC-DEC binary solvent, integral peak of PF6<sup>-</sup> stretching and peak center *versus* X<sub>Li</sub><sup>+</sup>, comparison of the SERS and IR spectra of various LiPF<sub>6</sub> in EC-DEC binary solvents in EC ring skeletal deformation region, peak deconvolution, pure spectral components for PCA and MCR analysis, MD simulations (PDF)> This material is available free of charge via the Internet at http://pubs.acs.org.

## REFERENCES

- 1. Gauthier, M.; Carney, T. J.; Grimaud, A.; Giordano, L.; Pour, N.; Chang, H.-H.; Fenning, D. P.; Lux, S. F.; Paschos, O.; Bauer, C., Electrode–Electrolyte Interface in Li-Ion Batteries: Current Understanding and New Insights. *J. Phys. Chem. Lett.* **2015**, *6*, 4653-4672.
- 2. Xu, K.; von Cresce, A.; Lee, U., Differentiating Contributions to "Ion Transfer" Barrier from Interphasial Resistance and Li<sup>+</sup> Desolvation at Electrolyte/Graphite Interface. *Langmuir* **2010,** *26*, 11538-11543.
- 3. Bard, A. J.; Faulkner, L. R.; Leddy, J.; Zoski, C. G., *Electrochemical Methods: Fundamentals and Applications*. Wiley New York: 1980; Vol. 2.
- 4. Peled, E., The Electrochemical Behavior of Alkali and Alkaline Earth Metals in Nonaqueous Battery Systems—the Solid Electrolyte Interphase Model. *J. Electrochem. Soc.* **1979,** *126*, 2047-2051.
- 5. Li, Y.; Li, Y.; Pei, A.; Yan, K.; Sun, Y.; Wu, C.-L.; Joubert, L.-M.; Chin, R.; Koh, A. L.; Yu, Y., Atomic Structure of Sensitive Battery Materials and Interfaces Revealed by Cryo—Electron Microscopy. *Science* **2017**, *358*, 506-510.
- 6. Sacci, R. L.; Black, J. M.; Balke, N.; Dudney, N. J.; More, K. L.; Unocic, R. R., Nanoscale Imaging of Fundamental Li Battery Chemistry: Solid-Electrolyte Interphase Formation and Preferential Growth of Lithium Metal Nanoclusters. *Nano Lett.* **2015**, *15*, 2011-2018.
- 7. Hell, S. W., Far-Field Optical Nanoscopy. *Science* **2007**, *316*, 1153-1158.
- 8. Lewis, I. R.; Edwards, H., *Handbook of Raman Spectroscopy: From the Research Laboratory to the Process Line*. CRC Press: 2001.

- 9. Everall, N. J., Confocal Raman Microscopy: Why the Depth Resolution and Spatial Accuracy Can Be Much Worse Than You Think. *Appl. Spectmsc.* **2000**, *54*, 1515-1520.
- 10. Campion, A.; Kambhampati, P., Surface-Enhanced Raman Scattering. *Chem. Soc. Rev.* **1998,** *27*, 241-250.
- 11. Nie, S.; Emory, S. R., Probing Single Molecules and Single Nanoparticles by Surface-Enhanced Raman Scattering. *Science* **1997**, *275*, 1102-1106.
- 12. Tian, Z.-Q.; Ren, B.; Wu, D.-Y., Surface-Enhanced Raman Scattering: From Noble to Transition Metals and from Rough Surfaces to Ordered Nanostructures. ACS Publications: 2002.
- Wu, D.; Xie, Y.; Ren, B.; Yan, J.; Mao, B.; Tian, Z., Surface Enhanced Raman Scattering from Bare Cobalt Electrode Surfaces. *PhysChemComm* **2001**, *4*, 89-91.
- 14. Yang, K.-H.; Liu, Y.-C.; Yu, C.-C., Simple Strategy to Improve Surface-Enhanced Raman Scattering Based on Electrochemically Prepared Roughened Silver Substrates. *Langmuir* **2010**, *26*, 11512-11517.
- 15. Zeng, Z.-C.; Huang, S.-C.; Wu, D.-Y.; Meng, L.-Y.; Li, M.-H.; Huang, T.-X.; Zhong, J.-H.; Wang, X.; Yang, Z.-L.; Ren, B., Electrochemical Tip-Enhanced Raman Spectroscopy. *J. Am. Chem. Soc.* **2015**, *137*, 11928-11931.
- 16. Li, J. F.; Huang, Y. F.; Ding, Y.; Yang, Z. L.; Li, S. B.; Zhou, X. S.; Fan, F. R.; Zhang, W.; Zhou, Z. Y.; Ren, B., Shell-Isolated Nanoparticle-Enhanced Raman Spectroscopy. *Nature* **2010**, *464*, 392-395.
- 17. Ko, H.; Singamaneni, S.; Tsukruk, V. V., Nanostructured Surfaces and Assemblies as SERS Media. *Small* **2008**, *4*, 1576-1599.
- 18. Yang, G.; Hallinan Jr, D. T., Self-Assembly of Large-Scale Crack-Free Gold Nanoparticle Films Using a 'Drain-to-Deposit' strategy. *Nanotechnology* **2016**, *27*, 225604.
- 19. Yang, G.; Hallinan, D. T., Gold Nanoparticle Monolayers from Sequential Interfacial Ligand Exchange and Migration in a Three-Phase System. *Sci. Rep.* **2016**, *6*, 35339.
- 20. Yang, G.; Nanda, J.; Wang, B.; Chen, G.; Hallinan, D. T., Self-Assembly of Large Gold Nanoparticles for Surface-Enhanced Raman Spectroscopy. *ACS Appl. Mater. Interfaces* **2017**.
- 21. Michaels, A. M.; Nirmal, M.; Brus, L., Surface Enhanced Raman Spectroscopy of Individual Rhodamine 6g Molecules on Large Ag Nanocrystals. *J. Am. Chem. Soc.* **1999**, *121*, 9932-9939.
- 22. Schroder, K. W.; Dylla, A. G.; Bishop, L. D.; Kamilar, E. R.; Saunders, J.; Webb, L. J.; Stevenson, K. J., Effects of Solute–Solvent Hydrogen Bonding on Nonaqueous Electrolyte Structure. *J. Phys. Chem. Lett.* **2015**, *6*, 2888-2891.
- 23. Morita, M.; Asai, Y.; Yoshimoto, N.; Ishikawa, M., A Raman Spectroscopic Study of Organic Electrolyte Solutions Based on Binary Solvent Systems of Ethylene Carbonate with Low Viscosity Solvents Which Dissolve Different Lithium Salts. *J. Chem. Soc., Faraday Trans.* **1998,** *94*, 3451-3456.
- 24. Han, S.-D.; Yun, S.-H.; Borodin, O.; Seo, D. M.; Sommer, R. D.; Young Jr, V. G.; Henderson, W. A., Solvate Structures and Computational/Spectroscopic Characterization of LiPF<sub>6</sub> Electrolytes. *J. Phys. Chem. C* **2015**, *119*, 8492-8500.
- 25. Yang, G.; Hu, L.; Keiper, T. D.; Xiong, P.; Hallinan, D. T., Gold Nanoparticle Monolayers with Tunable Optical and Electrical Properties. *Langmuir* **2016**, *32*, 4022-4033.
- 26. Giorgini, M. G.; Futamatagawa, K.; Torii, H.; Musso, M.; Cerini, S., Solvation Structure around the Li<sup>+</sup> Ion in Mixed Cyclic/Linear Carbonate Solutions Unveiled by the Raman Noncoincidence Effect. *J. Phys. Chem. Lett.* **2015**, *6*, 3296-3302.

- 27. Cazzanelli, E.; Croce, F.; Appetecchi, G. B.; Benevelli, F.; Mustarelli, P., Li<sup>+</sup> Solvation in Ethylene Carbonate–Propylene Carbonate Concentrated Solutions: A Comprehensive Model. *J. Chem. Phys.* **1997**, *107*, 5740-5747.
- 28. Sun, M.; Fang, Y.; Zhang, Z.; Xu, H., Activated Vibrational Modes and Fermi Resonance in Tip-Enhanced Raman Spectroscopy. *Physical Review E* **2013**, *87*, 020401.
- 29. Allen, J. L.; Borodin, O.; Seo, D. M.; Henderson, W. A., Combined Quantum Chemical/Raman Spectroscopic Analyses of Li<sup>+</sup> Cation Solvation: Cyclic Carbonate Solvents—Ethylene Carbonate and Propylene Carbonate. *J. Power Sources* **2014**, *267*, 821-830.
- 30. Fortunato, B.; Mirone, P.; Fini, G., Infrared and Raman Spectra and Vibrational Assignment of Ethylene Carbonate. *Spectrochim. Acta, Part A* **1971,** *27*, 1917-1927.
- 31. Aroca, R.; Nazri, M.; Nazri, G.; Camargo, A.; Trsic, M., Vibrational Spectra and Ion-Pair Properties of Lithium Hexafluorophosphate in Ethylene Carbonate Based Mixed-Solvent Systems for Lithium Batteries. *J. Solution Chem.* **2000**, *29*, 1047-1060.
- 32. Schroder, K.; Alvarado, J.; Yersak, T. A.; Li, J.; Dudney, N.; Webb, L. J.; Meng, Y. S.; Stevenson, K. J., The Effect of Fluoroethylene Carbonate as an Additive on the Solid Electrolyte Interphase on Silicon Lithium-Ion Electrodes. *Chem. Mater.* **2015**, *27*, 5531-5542.
- 33. Ding, S.-Y.; Yi, J.; Li, J.-F.; Ren, B.; Wu, D.-Y.; Panneerselvam, R.; Tian, Z.-Q., Nanostructure-Based Plasmon-Enhanced Raman Spectroscopy for Surface Analysis of Materials. *Nat. Rev. Mater.* **2016,** *I*, 16021.
- 34. Klassen, B.; Aroca, R.; Nazri, M.; Nazri, G., Raman Spectra and Transport Properties of Lithium Perchlorate in Ethylene Carbonate Based Binary Solvent Systems for Lithium Batteries. *J. Phys. Chem. B* **1998**, *102*, 4795-4801.
- 35. Ue, M.; Sasaki, Y.; Tanaka, Y.; Morita, M., Nonaqueous Electrolytes with Advances in Solvents. In *Electrolytes for Lithium and Lithium-Ion Batteries*, Springer: 2014; pp 93-165.
- 36. Xu, K., Electrolytes and Interphases in Li-Ion Batteries and Beyond. *Chem. Rev.* **2014**, 114, 11503-11618.
- 37. Seo, D. M.; Reininger, S.; Kutcher, M.; Redmond, K.; Euler, W. B.; Lucht, B. L., Role of Mixed Solvation and Ion Pairing in the Solution Structure of Lithium Ion Battery Electrolytes. *J. Phys. Chem. C* **2015**, *119*, 14038-14046.
- 38. Durig, J. R.; Clark, J. W.; Casper, J. M., Vibrational Spectra and Structure of Small Ring Compounds. *J. Mol. Struct.* **1970,** *5*, 67-84.
- 39. Nie, M.; Abraham, D. P.; Seo, D. M.; Chen, Y.; Bose, A.; Lucht, B. L., Role of Solution Structure in Solid Electrolyte Interphase Formation on Graphite with LiPF<sub>6</sub> in Propylene Carbonate. *J. Phys. Chem. C* **2013**, *117*, 25381-25389.
- 40. Chapman, N.; Borodin, O.; Yoon, T.; Nguyen, C. C.; Lucht, B. L., Spectroscopic and Density Functional Theory Characterization of Common Lithium Salt Solvates in Carbonate Electrolytes for Lithium Batteries. *J. Phys. Chem. C* **2017**, *121*, 2135-2148.
- 41. Borodin, O.; Olguin, M.; Ganesh, P.; Kent, P. R.; Allen, J. L.; Henderson, W. A., Competitive Lithium Solvation of Linear and Cyclic Carbonates from Quantum Chemistry. *Phys. Chem. Chem. Phys.* **2016**, *18*, 164-175.
- 42. Lee, K.-K.; Park, K.; Lee, H.; Noh, Y.; Kossowska, D.; Kwak, K.; Cho, M., Ultrafast Fluxional Exchange Dynamics in Electrolyte Solvation Sheath of Lithium Ion Battery. *Nat. Commun.* **2017**, *8*, 14658.
- 43. von Cresce, A.; Xu, K., Preferential Solvation of Li<sup>+</sup> Directs Formation of Interphase on Graphitic Anode. *Electrochem. Solid-State Lett.* **2011**, *14*, A154-A156.

- 44. Bogle, X.; Vazquez, R.; Greenbaum, S.; Cresce, A. v. W.; Xu, K., Understanding Li<sup>+</sup>– Solvent Interaction in Nonaqueous Carbonate Electrolytes with <sup>17</sup>O NMR. *J. Phys. Chem. Lett.* **2013**, *4*, 1664-1668.
- 45. Lucht, B. L. C., David B, Hexamethyldisilazide, Lithium: A View of Lithium Ion Solvation through a Glass-Bottom Boat. *Acc. Chem. Res.* **1999**, *32*, 1035-1042.
- 46. Ganesh, P.; Jiang, D.-E.; Kent, P., Accurate Static and Dynamic Properties of Liquid Electrolytes for Li-Ion Batteries from Ab Initio Molecular Dynamics. *J. Phys. Chem. B* **2011**, *115*, 3085-3090.
- 47. Shakourian-Fard, M.; Kamath, G.; Sankaranarayanan, S. K., Evaluating the Free Energies of Solvation and Electronic Structures of Lithium-Ion Battery Electrolytes. *ChemPhysChem* **2016**, *17*, 2916-2930.
- 48. Xu, K., Nonaqueous Liquid Electrolytes for Lithium-Based Rechargeable Batteries. *Chem. Rev.* **2004**, *104*, 4303-4418.
- 49. Banik, M.; El-Khoury, P. Z.; Nag, A.; Rodriguez-Perez, A.; Guarrottxena, N.; Bazan, G. C.; Apkarian, V. A., Surface-Enhanced Raman Trajectories on a Nano-Dumbbell: Transition from Field to Charge Transfer Plasmons as the Spheres Fuse. *ACS Nano* **2012**, *6*, 10343-10354.
- 50. Borodin, O.; Suo, L.; Gobet, M.; Ren, X.; Wang, F.; Faraone, A.; Peng, J.; Olguin, M.; Schroeder, M.; Ding, M. S., Liquid Structure with Nano-Heterogeneity Promotes Cationic Transport in Concentrated Electrolytes. *ACS Nano* **2017**, *11*, 10462-10471.
- 51. Vatamanu, J.; Borodin, O.; Smith, G. D., Molecular Dynamics Simulation Studies of the Structure of a Mixed Carbonate/LiPF<sub>6</sub> Electrolyte near Graphite Surface as a Function of Electrode Potential. *J. Phys. Chem. C* **2011**, *116*, 1114-1121.
- 52. Halgren, T. A., Merck Molecular Force Field. Ii. Mmff94 Van Der Waals and Electrostatic Parameters for Intermolecular Interactions. *J. Comput. Chem.* **1996,** *17*, 520-552.

# Table of Contents

